III-V INVERSE QUANTUM DOTS FABRICATION, CHARACTERIZATION AND APPLICATION

BY

JEONG DONG KIM

THESIS

Submitted in partial fulfillment of the requirements
for the degree of Master of Science in Electrical and Computer Engineering
in the Graduate College of the
University of Illinois at Urbana-Champaign, 2013

Urbana, Illinois

Adviser:

Professor James J. Coleman

ABSTRACT

The quantum dot offers carrier confinement in three dimensions. It is expected to improve performance of photonic devices. However, quantum dot fabrication still requires significant quality improvement such as high uniformity and location controllability to be commercialized.

In this thesis, the inverse quantum dot is presented as an alternative solution to enhance the quality of conventional quantum dots. The theoretical analysis shows that the inverse quantum dot can be tuned from quantum well to quantum dot like behavior by decreasing the pitch and increasing the diameter of pores. The inverse quantum dots are made with four basic processing steps: base structure growth, dielectric film patterning, etching, and regrowth. Electron beam lithography is used to increase the uniformity of the dots. Scanning electron microscopy shows the highly ordered pores compared to self-assembled quantum dots. The photoluminescence characterization shows the increased intensity compared to quantum well. Also, the quantization effect in the photoluminescence characterization shows the quantum dot like phenomenon.

Diblock copolymer lithography and anodic aluminum oxide transfer are used to fabricate large area dot patterning. In diblock copolymer lithography, pore diameter and pitch are approximately 17 nm and 37 nm respectively. In anodic aluminum oxide transfer, pore diameter and pitch were approximately 140 nm and 500 nm respectively. These two techniques indicate their capability in performing large area quantum dot and inverse quantum dot fabrication.

To Sang Tae Kim and Kyeung Ae Park, for their unconditional love and support

ACKNOWLEDGMENTS

First of all, I want to thank Prof. James Coleman for giving me an opportunity to research. Jim not only taught me how to be a true researcher, but also advised me with innumerable life lessons. Jim ignited my passion to learn new knowledge. If I had not meet Jim, I would never have understood the enjoyment of learning. I will never forget his trust and support of me. I also want to offer thanks to Neville Dias, Uttam Reddy, Akash Garg, and Jonathan Young for introducing me to cleanroom tools. Without them, I would not know how to fabricate any devices. I also want to thank Uguen Choi for going through all those hard times with me when we were the only students left in the lab. I also want to thank Joe Zimmerman for helping me and Uguen Choi to learn about and set up the test equipment. Thanks also go to Yun Lu, Pavel Liudvih, Shiul Khadka, and Runyu Liu for helping me on research and for their friendship. I also want to thank to Prof. Ann Catrina Coleman, Prof. Xiuling Li, and Dr. Oliver Chen for giving me ideas and advice on research. Thanks go to Prof. Xiuling Li's group members including Parsian Mohseni, Paul Froeter, Kevin Basset, Ryan Dowdy, Xin Miao, Chen Zhang, and Kyooho Jung for helping me whenever I stepped into the office to ask questions about growth. Finally, I want to thank my parents Sang Tae Kim and Kyeung Ae Park and my brother Ho Dong Kim for their endless support and their love. Without them, I am nothing. I truly love my family and I will work with all my effort to make them happy.

CONTENTS

1. INTRODUCTION

Quantum dot (QD) based photonic devices benefit from three-dimensional spatial confinement, exhibiting great tenability and enhanced performance as compared to those based on other less confined structures such as the bulk, the quantum well (QW), and the quantum wire. The semiconductor laser diode with QD active region has been widely researched due to its potential advantage of having a delta-function-like density of states (DOS). Reported QD lasers show wider emission wavelength tunability, lower threshold current density, and higher temperature stability [1], [2], [3], [4], [5]. QD photovoltaic devices are also actively studied. Multiple exciton generation (MEG) and intermediate band (IB) gap solar cell produced from the QD suggest even higher efficiency for solar energy harvesting [6], [7], [8]. The number of commercialized QD products has been increasing exponentially over the years.

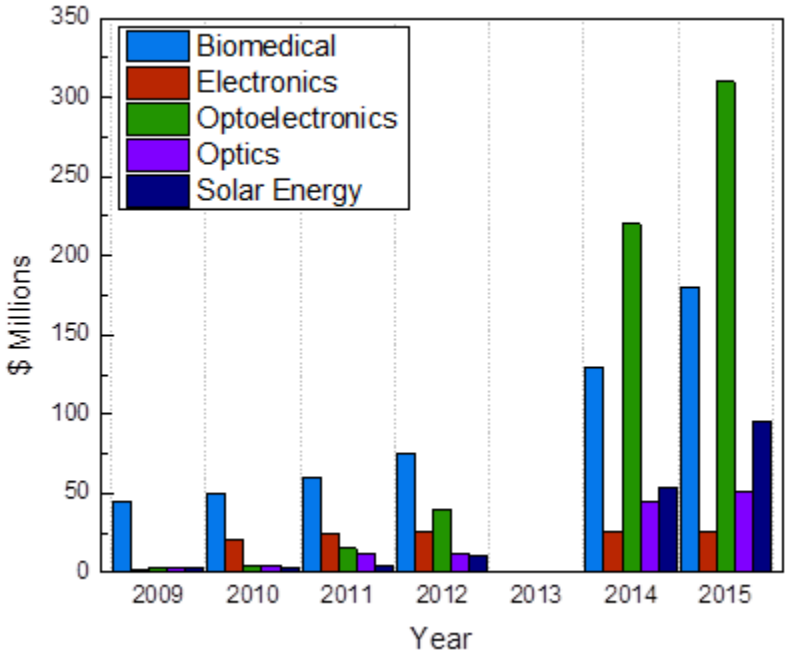

Figure 1.1 Quantum dots market analysis from 2009 to 2015 [9].

Figure 1.1 shows a market analysis of the QD industry reported by BCC research. According to this research, the overall QD market in the year 2010 was $67M in estimated total revenue. The QD market is expected to reach approximately $610M by the year 2015 which is a compound annual growth rate (CAGR) of 59.3 percent. The optoelectronic field is expected to have the largest share of the QD market in the year 2015. This field is expected to reach approximately $310M with the CAGR of 128.4 percent by the year 2015 [9].

The successful commercialization of QD devices critically depends on the yield and the cost of the QD fabrication. For high yield, the QD product must fulfill three conditions that reflect size, uniformity, and material quality. If the QD size does not satisfy the requirement of the zero dimensional structure, it cannot confine the carriers in all three dimensions. If the QDs in the lattice do not have high uniformity, the electrical and optical properties would not match from one dot to the other. If there are undesired defects or impurities, the advantages of the zero-dimensional structure will not be achieved. The optimal fabrication process is the key factor for satisfying the aforementioned conditions. Self-assembly and selective area epitaxy (SAE) are two examples of a bottom-up QD growth process. The details of the bottom-up QD growth process are described in Section 1.2.

The properties of fabricated QDs typically do not exactly match those of theoretical ones. The major problems are homogeneous and inhomogeneous broadening of the quantized states in the fabricated QD which results in severe performance degradation. For instance, broadening makes a QD semiconductor diode laser have higher threshold current density, degrades high temperature stability, and broadens linewidth emission spectrum [1], [2], [10]. Different fabrication methods are intensively researched in order to alleviate the broadening

problem. In this thesis, the Inverse quantum dot (IQD) array structure is introduced as an alternative solution. Before going into the details of this advanced zero-dimensional structure, I will briefly go over the traditional confined structures, the existing QD fabrication methods, and the broadening issues in general.

1.1 Density of States

The density of states (DOS) describes the number of available energy states per unit energy per unit volume of the material. As the confinement changes from 3D to 0D, the DOS of the material also changes [11]. Figure 1.2 plots typical functional relationship the plot of DOS vs. energy.

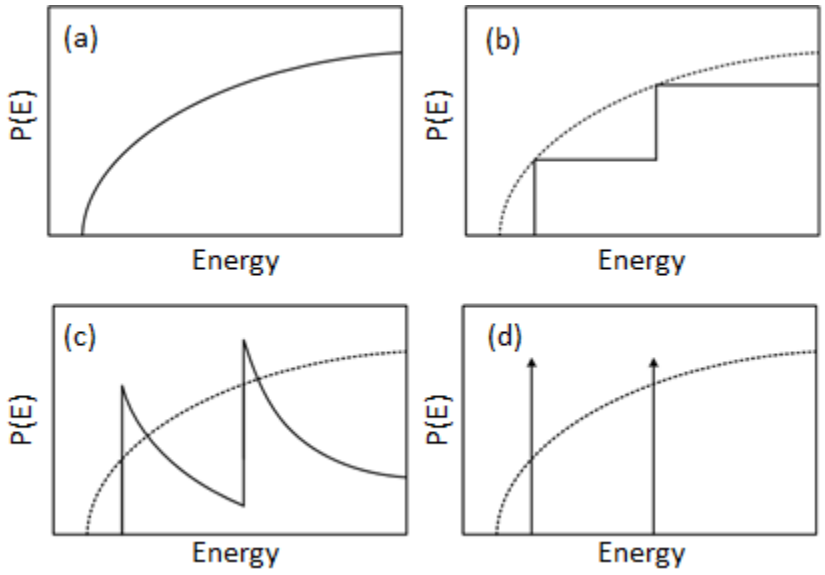

Figure 1.2 Density of states of (a) bulk, (b) quantum well, (c) quantum wire and (d) quantum dot.

In bulk structure, the DOS is proportional to the square root of the energy as shown in Figure 1.2 (a). The QW is the structure in which one out of three dimensions is smaller than the de Broglie wavelength of the material. In the QW, the DOS is expressed:

$$\rho_{2D}(E) = \frac{m^*}{\pi\hbar^2 L_z} \sum_n H(E - E_n) \tag{1.1}$$

where m^* is the electron effective mass, L_z is the thickness of the QW, E_n is the energy at nth state, and $H(E - E_n)$ is the Heaviside step function.

When two dimensions of the structure become smaller than the de Broglie wavelength of the material, the structure is called a quantum wire. The DOS of the quantum wire is inversely proportional to the square root of energy as shown in Figure 1.2 (c). Note that for particular levels of the energy, the DOS for a quantum wire exceeds that of the bulk structure. This makes quantum wire devices have higher sensitivity.

When all three dimensions of the structure become smaller than the de Broglie wavelength of the material, the structure is called a QD. The QD DOS is represented by the delta function as shown in Figure 1.2 (d).

Unlike the bulk structure, structures like the QW, quantum wire, and QD provide carrier confinement along one or more dimensions. The emission and absorption spectra of the structure can be tuned by varying its size. The carrier confinement becomes stronger as the size of the confined dimension becomes smaller, and the energy separation between the ground and the excited state increases accordingly.

The electron concentration can be derived from the DOS as shown in equation (1.2).

$$n = \int_{\infty}^{\infty} f(E)\rho(E)\,dE \tag{1.2}$$

The term $f(E)$ is the Fermi-Dirac distribution. The Fermi-Dirac distribution integrated over the DOS gives the number of the electrons in a particular energy state. This value integrated over all of the available energy states number is the total carrier concentration in the material.

1.2 III-V Quantum Dots

III-V materials are important for photonic devices. Most III-V compounds are direct band gap materials, which exhibit much higher light emission or absorption efficiency than indirect bandgap semiconductors such as silicon or germanium. Another advantage of III-V compounds is the ability to tune the bandgap by introducing lattice mismatched alloy. III-V binary compounds such as GaAs or InP have the energy bandgaps of 1.43 eV and 1.35 eV which correspond to 867 nm and 918 nm. However, ternary compounds such as $In_xGa_{1-x}As$ and have bandgaps that can be tuned over a range of wavelengths μm, which is the most important wavelength channel for optical data transmission.

The ideal III-V QD has delta-like DOS as discussed in Section 1.1. However, actual III-V QD arrays have different characteristics due to the limits of controllability in the QD fabrication processes. Fabricated QDs may have slightly different dimensions. There may also be defects in the lattice formed by the QDs. Both of these imperfections in fabrication may introduce fluctuation of the optical properties of individual QD, which eventually leads to inhomogeneous broadening of the light emission spectrum of the device. The fabrication methods and related problems will be discussed in the following sections.

1.2.1 Self-Assembled Growth

Three basic bottom-up growth mechanisms are the Frank-van der Merwe (FvdM), Stranski-Krastanov (SK), and Volmer-Weber (VW) mechanisms. Growth modes are first introduced by Bauer in 1958 [12]. These mechanisms are distinguished by the strain energy between the substrate and the grown layer. FvdM growth occurs when the growth material is the same as the substrate material. In this case, no strain energy exists between them. When lattice mismatched material is grown on top of substrate, strain energy is introduced. The strain in the grown layer becomes either tensile or compressive depending on the strain energy as shown in equation (1.3).

$$f = \pm \left| \frac{\Delta a_0}{a_0} \right| \tag{1.3}$$

where a_0 is the lattice constant of the substrate, and Δa_0 is the lattice constant difference between the substrate and the grown layers. If the strain energy is positive, the grown layer becomes a compressive layer and if it is negative then the layer becomes a tensile layer.

As the layer grows thicker, the strain energy between the substrate and the grown layer increases. As the layer reaches the critical thickness, the strain energy relaxes by formation of misfit dislocations [12], [13], [14]. Equation (1.4) describes the critical thickness of the layer.

$$h_c = \frac{a_0}{2\sqrt{2}\pi f} \frac{(1-0.25v)}{(1+v)} \left(\ln \frac{h_c \sqrt{2}}{a_0} + 1 \right) \tag{1.4}$$

where f is the misfit energy calculated from the equation (1.3). The parameter v is the Poisson's ratio described by the equation (1.5)

$$v = \frac{c_{12}}{c_{11} + c_{12}} \tag{1.5}$$

where C_{11} and C_{12} are the elastic coefficients of the materials. If the lattice mismatch induces strong strain energy, then VW mechanism occurs.

Self-assembled QDs are grown using the SK growth mechanism. The size and density of self-assembled QDs can be controlled by adjusting the flow rate of the metal-organic source vapor, the growth temperature, and other parameters. The size of a single QD can be controlled down to several nanometers. However, it is difficult to individually control the size and the location of the QD in the array. Therefore, the variation of the QD sizes leads to different quantization energy in the ground and the excited states.

1.2.2 Selective Area Epitaxy

SAE QDs have been considered in order to reduce the QD size fluctuation and to define their precise distribution in the array. SAE uses a patterned dielectric film as the mask layer to define the growth regions. MOCVD SAE involves two different diffusion mechanisms: vapor-phase diffusion and surface diffusion [15], [16], [17], [18]. The precursor's diffusion rates are different above the patterned and non-patterned substrate areas. The vapor-phase diffusion has diffusion lengths of approximately 100 μm. The surface diffusion has diffusion lengths of approximately 1 μm. Therefore, vapor-phase diffusion dominates in the growth when the mask opening width is more than 100 μm [19]. Vapor-phase diffusion has the large precursor modulation which results in the growth rate and the composition enhancement [20], [21], [22]. For SAE QDs, dielectric film openings are on the order of a few hundred nanometers; thus, surface diffusion dominates.

Defining the area of self-assembled InAs QDs using the SAE has been reported by Yeoh in 2000 [23]. In this report, InAs QDs were selectively grown on $In_{0.2}Ga_{0.8}As$ QW regions using

the atmospheric pressure MOCVD. QDs with density of 3.1×10^{12} cm^{-2} were fabricated in the $In_{0.2}Ga_{0.8}As$ region. The SAE method of InAs QDs fabrication using a patterned dielectric film was reported by Dias et al. in 2011 [24]. In this report, an SiO_2 dielectric film is patterned using electron beam lithography. QDs having 1.8×10^{10} cm^{-2} density were fabricated with a diameter of 50 nm and a pitch of 80 nm. Reducing the size fluctuation by controlling the diameter, height, and the pitch of the dots decreases homogeneous broadening.

1.2.3 Homogeneous and Inhomogeneous Broadening

As discussed in earlier sections, the DOS of the fabricated QDs has homogeneous and inhomogeneous broadening. This broadening can be seen in the emission linewidth of the semiconductor diode laser. Homogeneous broadening is produced by nonradiative decay and dephasing collisions [25], [26]. The broadening caused by nonradiative decay is called T_1 broadening and is caused by the collisions between the free carrier and the surrounding atoms. Let us define *u* and *l* to be a particular upper energy level and a lower energy level respectively. Then the decay rates can be expressed as shown in equations (1.6) and (1.7).

$$\gamma_1^u = \sum_i A_{ui} + \frac{1}{T_1^u} \tag{1.6}$$

$$\gamma_1^l = \sum_j A_{lj} + \frac{1}{T_1^l} \tag{1.7}$$

where γ_u and γ_l are the decay rates and T_1^u and T_1^l are the carrier decay time in the energy states *u* and *l*. The broadened emission linewidth, $\Delta\nu_{ul}$ can be derived as shown in equation (1.8).

$$\Delta v_{ul} = \frac{1}{2\pi}\left[\left(\sum_i A_{ui} + \sum_j A_{lj}\right) + \frac{1}{T_1^u} + \frac{1}{T_1^l}\right] \tag{1.8}$$

The summations indicate the total decay rate of the upper and lower states induced by the natural emission. The emission linewidth of the laser broadens when the nonradiative decay time is shorter than the radiative decay time.

The broadening caused by dephasing collisions is called the T_2 broadening. The collisions between the free carriers and atoms produce an ensemble phase interruption and this results the T_2 broadening. The emission spectrum has Lorentzian distribution when the dephasing collisions dominate in the structure. The decay rates of the energy state *u*, and the lower state *l* are shown in the equations (1.9) and (1.10).

$$\gamma_2^u = \frac{1}{T_2^u} \tag{1.9}$$

$$\gamma_2^l = \frac{1}{T_2^l} \tag{1.10}$$

where T_2^u and T_2^l are the average time between phase interrupting collisions in the state *u* and *l*. The overall homogeneous broadening caused by the nonradiative decay and the dephasing collisions is derived from the equations (1.6) to (1.10) and is shown in the equation (1.11).

$$\Delta v_{ul} = \frac{1}{2\pi}\left[\left(\sum_i A_{ui} + \sum_j A_{lj}\right) + \frac{1}{T_1^u} + \frac{1}{T_1^l} + \frac{2}{T_2}\right] \tag{1.11}$$

The inhomogeneous broadening is caused by the fluctuation of the QD size. The size variation results in different number of energy levels in dots. Since the QD does not share the carrier pool with other dots, different size QDs produce an ensemble spectrum that has the Gaussian distribution.

The changes in the DOS due to broadening are shown in Figure 1.3. The delta function like DOS of the ideal single QD is shown in Figure 1.3 (a). The Gaussian distribution due to inhomogeneous broadening is shown in Figure 1.3 (b). The Lorentzian distributions of each QD are shown in Figure 1.3 (c). The experimental analysis of the effect of the inhomogeneous broadening in the QD semiconductor laser was reported by Asryan and Suris in 1995 [10]. The report attributes the cause for increased threshold current density of the QD laser to the inhomogeneous broadening.

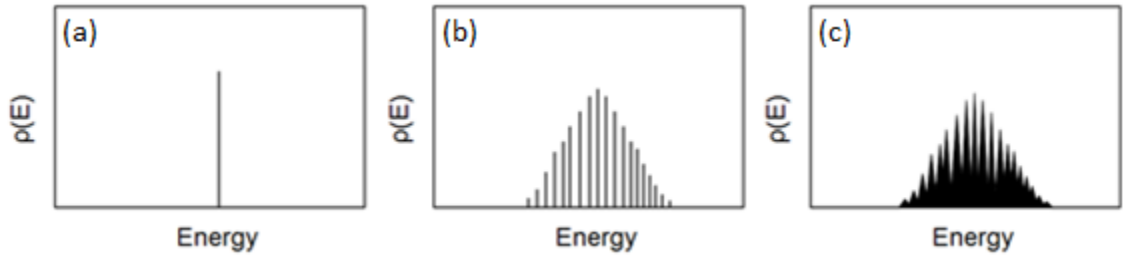

Figure 1.3 Density of states of (a) ideal QD, (b) QD with inhomogeneous broadening, (c) QD with both homogeneous and inhomogeneous broadening.

The temperature dependence and the effect of the homogeneous broadening in the QD semiconductor laser has been theoretically and experimentally reported by Sugawara in 1997 and 2000 [27], [28]. The results from these papers show that the homogeneous broadening decreases as the temperature decreases. This is due to the reduction of the carrier to carrier scattering, and the free carrier to atom scattering. At room temperature, the homogeneous broadening dominates and reduces the peak of the DOS. This effect increases the threshold current density of the diode laser [29].

2. III-V INVERSE QUANTUM DOT (IQD)

As described in Chapter 1, homogeneous and inhomogeneous broadening degrades the performance of QD based devices. Homogeneous broadening due to carrier and phonon collision and dephasing can be alleviated by cooling the device to cryo temperatures. Size fluctuations in the QD array can be reduced through further development and perfection of the fabrication technology. In this chapter, I will introduce an alternative zero-dimensional structure, the inverse quantum dot (IQD), which possesses some favorable properties as compared to traditional QDs. The fabrication process is described in Section 2.1 and theoretical and experimental analyses are described in Sections 2.2 and 2.3 respectively.

2.1 Structure

The IQD is a two dimensionally periodically modulated lower energy bandgap material sandwiched between higher energy bandgap top and bottom barrier layers. In the structure, a QW of lower energy band gap material is patterned with a 2D array of pores and these pores are filled with same higher energy bandgap material as that of the barrier layers. In the following theoretical and the experimental discussion of the IQD, GaAs and $In_xGa_{1-x}As$ are used. The energy bandgap of GaAs is 1.43 eV. The energy bandgap of $In_xGa_{1-x}As$ can be selected from 0.36 eV to 1.43 eV depending on the composition of indium. In IQD structure, each dot is formed from higher bandgap energy material. The cross-section view of IQD is shown in Figure 2.1.

$In_xGa_{1-x}As$ is the region where the carriers get confined. Depending on the in-plane dimensions of $In_xGa_{1-x}As$, IQD can be controlled to either QW or QD like structure. This can be

done by three variables that are diameter, pitch, and ordering of pores. When the diameter of the pore increases, and the pitch of the pores decreases, stronger quantization of the carriers can be achieved. In contrast to QDs which are spatially isolated from each other, IQDs are spatially connected. This connectivity allows IQDs to share the same carrier pool, thus reducing inhomogeneous broadening.

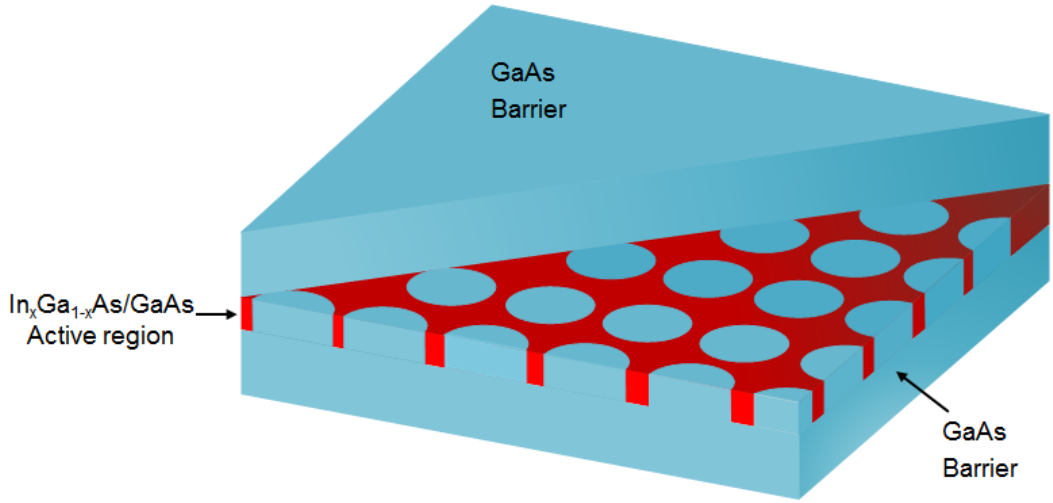

Figure 2.1 Tilted cross-section view of inverse quantum dot structure. Blue regions are GaAs material and red regions are $In_xGa_{1-x}As$ material.

The composition of $In_xGa_{1-x}As$ QW is limited by the amount of lattice mismatch with GaAs barrier layers. As composition of indium increases, the lattice mismatch also increases. This leads to stronger strain energy induced in the QW and limits its critical thickness. As mentioned in Section 1.2.1, if the strain energy is relaxed the growth material forms dislocations when the QW exceeds its critical thickness. Therefore, precise control of composition and thickness of the QW is required in the IQD structure. For the theoretical and experimental analysis, 19 percent and 31 percent indium compositions are used.

The limitation of our electron beam lithography facility restricts the controllability of parameters of IQD structure. The pitch of the pores can be controlled down to 80 nm and the pore diameter can be controlled to between 30 nm and 70 nm. IQD can be patterned either in a hexagonal or a square order. The areas between the pores are smaller in the hexagonal pattern.

2.2 Fabrication

There are nine fabrication steps to make an IQD structure for a photoluminesence (PL) characterization. These steps are shown in Figure 2.2.

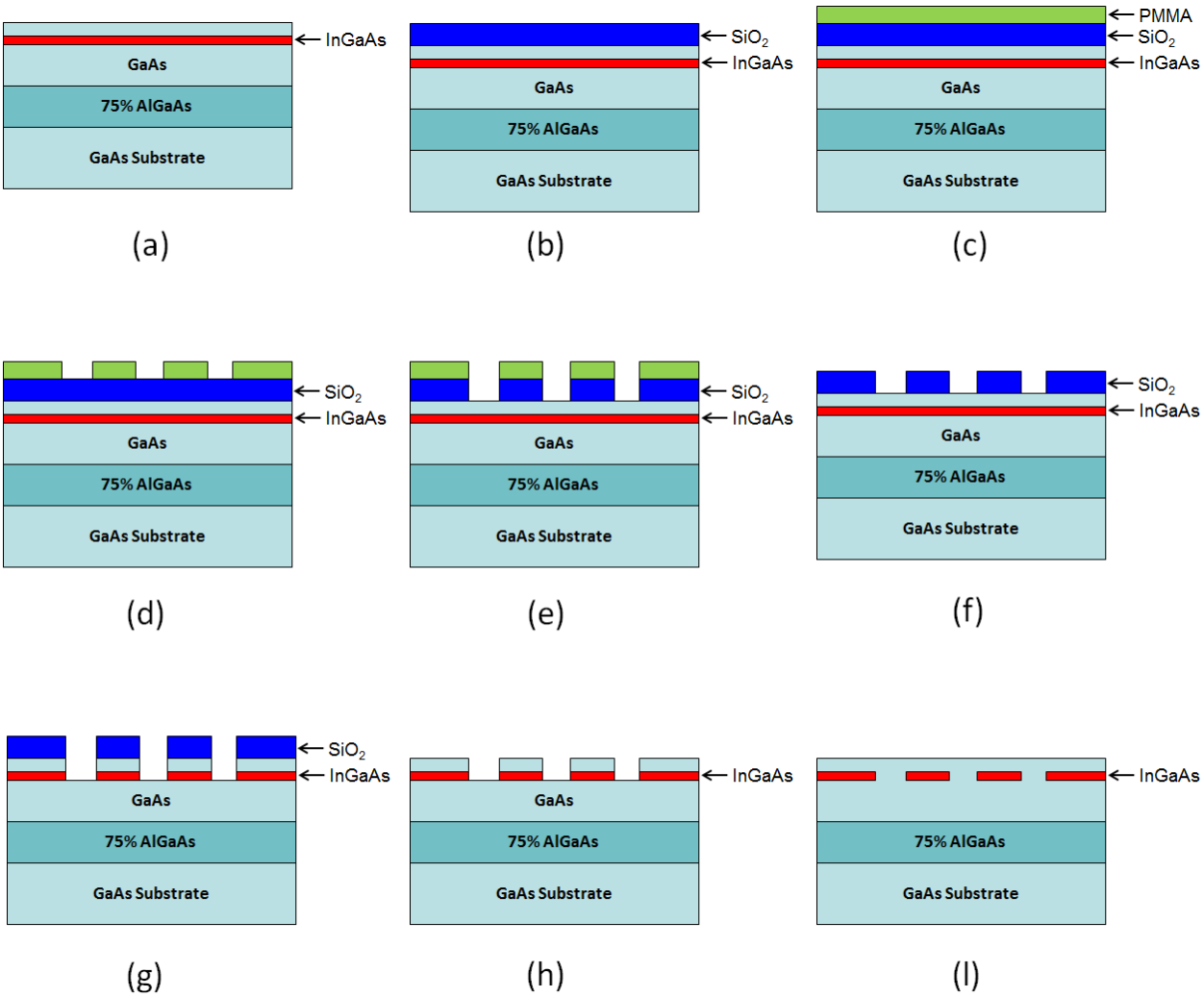

Figure 2.2 Fabrication process of IQD.

First, a base structure is grown on the <001> GaAs substrate using atmospheric pressure MOCVD. The base structure includes an $Al_{0.75}Ga_{0.25}As$ lower cladding layer, a GaAs barrier layer and the $In_{0.19}Ga_{0.81}As$ QW layer. There is also a thin GaAs layer on top of the QW to prevent oxidation and damage from the remaining process. Next, a 30 nm SiO_2 film is deposited using plasma enhanced vapor deposition (PECVD). This layer is used as a dielectric mask for dot patterning in the later steps. Then, a 1μm thick alignment mark is patterned at the edge of the sample using a conventional photolithography and Ti-Au deposition. This alignment mark serves as a reference for the electron beam lithography. Then, 950K poly-methyl-methacrylate (PMMA) is spin coated on top of the sample to serve as the electron beam lithography resist. The polymer layer is baked for 3 minutes at temperature of 210 ℃.

Diameter, pitch, and ordering of the pores are designed using CAD drawing or the JEOL coding. Then, the exposed PMMA is developed in IMBK:IPA solution for 30s. Next, patterns in the PMMA are transferred into the SiO_2 using Freon reactive ion etching (RIE). After etching, the PMMA sacrificial layer is removed with an acetone-methanol-IPA cleaning procedure. Also, O_2 descum is used to remove a residual PR on the sample surface. Next, the patterns in the SiO_2 dielectric mask are transferred by wet etching which consists of four steps. First, the sample is immersed in 1:10 NH_4OH:DI solution for 30 s for etching the native oxide. Then, a solution of 1:5:495 H_3PO_4:H_2O_2:DI is used to etch the GaAs capping layer and the $In_{0.19}Ga_{0.81}As$ active region. Since the active region is only 8.6 nm, precise time control is required. A typical etching rate using this solution is approximately 0.43 nm/s. After that, the sample is oxidized in H_2O_2 for 15 s, and etched in 1:1 HCL:DI for 15 s to remove the native oxide.

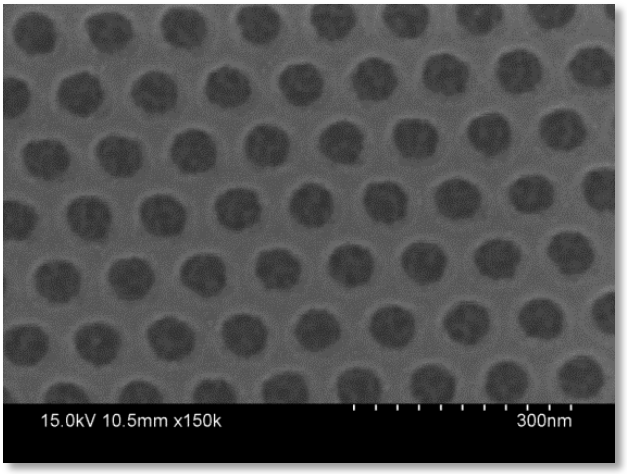

Figure 2.3 Scanning electron microscope (SEM) image.

After the wet etching process, the remaining SiO_2 film is etched using BHF. Figure 2.3 shows an SEM picture of the hexagonal ordering IQD active layer after the SiO_2 film etching. The pore diameter and pitch are approximately 60 nm and 100 nm. Next, GaAs is grown to fill the pores and to deposit the upper barrier layer. For the PL sample, a symmetrical upper cladding layer and a cap layer are grown.

2.3 Theoretical Analysis

In order to compare IQD and QD, it is necessary to derive and compare energy dispersion diagrams. Finite difference, finite element, and a partial function expansion methods are used to solve the dispersion relation of the structures [30], [31], [32]. A simplified calculation is also performed before using the advanced methods.

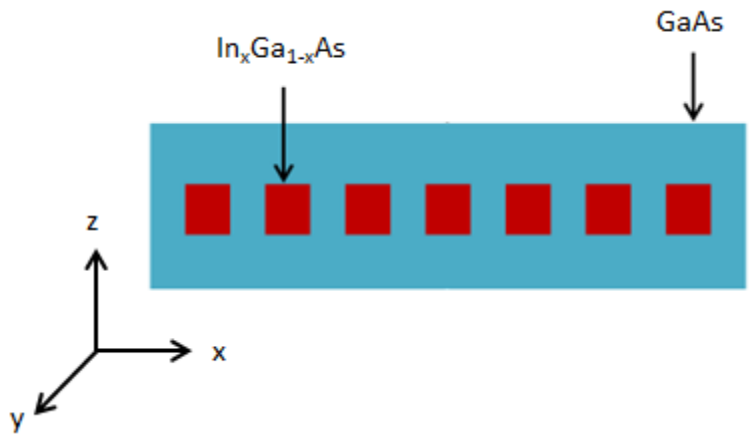

Figure 2.4 Cross-section view of IQD array structure from y (or x) direction

Figure 2.4 shows the cross-section view of an IQD array. The analysis of the structure can be divided into two parts: by looking at the structure along the z direction, and along the x-y directions. The energy band diagram along the z-direction is similar to a finite QW band diagram model. The energy band diagram of the well is shown in Figure 2.5, where E_c and E_v are the energy levels of conduction and valence bands, m_w^* and m_b^* are the effective masses of the carriers in the well and the barrier respectively, L_w is the thickness of the QW, C1, HH1 are the ground states of the conduction band and the heavy-hole band respectively.

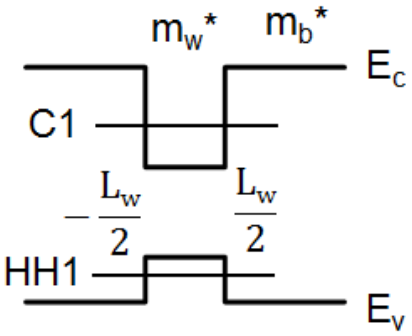

Figure 2.5 Energy band diagram of simple finite QW.

As described in Section 1.2, energy levels of ground and excited states can be controlled by varying the thickness of the QW.

As the QW thickness decreases, quantization of the carrier increases. The carrier wave function can be derived from the Schrödinger equation:

$$\psi(r) = \frac{e^{ik_t \cdot r}}{\sqrt{A}} \psi(z) \tag{2.1}$$

The Schrödinger equation can be simplified as

$$-\frac{\hbar^2}{2}\frac{\partial}{\partial z}\left[\frac{1}{m(z)}\frac{\partial}{\partial z}\psi(z)\right] + V(z)\psi(z) = \left(E(k_t) - \frac{\hbar^2 k_t^2}{2m(z)}\right)\psi(z) \tag{2.2}$$

From equation (2.2) the eigenvalue and the eigenfunction can be calculated and energy of the states in conduction band can be derived as

$$E_n(k_t) = E_n(0) + \frac{\hbar^2 k_t^2}{2m_w^*} \tag{2.3}$$

$E_n(0)$ is the quantized energy along the z-direction for the *n*th state when the transverse wave vector k_t = 0. The transverse wave vector can be represented in terms of x and y components $k_t^2 = k_x^2 + k_y^2$.

The energies of the heavy-hole and light-hole bands are described as shown in equations (2.4) and (2.5).

$$E_{HH}(k_z) = -\frac{\hbar^2}{2m_0}(\gamma_1 - 2\gamma_2)k_z^2 \tag{2.4}$$

$$E_{LH}(k_z) = -\frac{\hbar^2}{2m_0}(\gamma_1 + 2\gamma_2)k_z^2 \tag{2.5}$$

In equations (2.4) and (2.5), parameters γ_1 and γ_2 are Luttinger parameters [33], m_0 is the mass of the free electron. The effective heavy-hole and light-hole mass along the z-direction are expressed in terms of m_0 and Luttinger parameters.

$$m_{hh}^z = \frac{m_0}{\gamma_1 - 2\gamma_2} \tag{2.6}$$

$$m_{lh}^z = \frac{m_0}{\gamma_1 + 2\gamma_2} \tag{2.7}$$

For GaAs, γ_1 = 6.8, γ_2 = 1.9. For InAs, γ_1 = 20.4 γ_2 = 8.3.

The second case is when IQD is visualized along the x-y direction. In this case, the energy band diagram is similar to the two-dimensional Kronig-Penney model. The one-dimensional Kronig-Penney model for a superlattice structure is derived [34], [35]. The wave vector of a barrier is the imaginary part of the bound state solution of the one-dimensional Kronig-Penney model as shown in equations (2.8) and (2.9).

$$k_b = i\alpha_b \tag{2.8}$$

$$\alpha_b = \sqrt{\frac{2m_b}{\hbar^2}(V_0 - E)} \tag{2.9}$$

where m_b is the carrier effective mass in the barrier and V_0 is the potential drop across the barrier. The Kronig-Penney's parameter P is calculated as:

$$P = \frac{m_w k_b}{m_b k} = i\frac{m_w \alpha_b}{m_b k} = i\eta \tag{2.10}$$

where m_w is the carrier effective mass in the well. The determinant equation of the Kronig-Penney's model can be simplified as

$$\cos(qL) = f(E) \tag{2.11}$$

The solutions for the eigenequation $f(E)$ from (2.11) can be found as:

$$f(E)=\cos(kw)\cosh(\alpha_b b)+\frac{1}{2}\left(\eta-\frac{1}{\eta}\right)\sin(kw)\sinh(\alpha_b b) \qquad 0<E<V_0 \qquad (2.12)$$

$$f(E)=\cos(kw)\cosh(k_b b)-\frac{1}{2}\left(P-\frac{1}{P}\right)\sin(kw)\sinh(k_b b) \qquad V_0<E \qquad (2.13)$$

where w is the width of the well and b is the width of the barrier, $L=w+b$ is the length of one period. A graphical solution of the eigenequation can be found by plotting the equation (2.11). The $\cos(qL)$ on the left side of equation (2.11) limits $f(E)$ creating the discontinuity.

The discontinuous regions are forbidden energy gaps. Starting from the lowest energy level, the continuous regions indicate the first, second, and the third subbands of the conduction or valence bands. This means that by changing the widths of the well and the barrier, the energy level of each subband and the forbidden gap of the carriers can also be controlled. By changing the diameter and the pitch of the IQDs in the active region, the dispersion relation can be controlled.

In order to understand the complete energy dispersion diagram, IQD structure needs to be analyzed in all directions at the same time. As described in the previous section, there are several approaches to calculate the dispersion relationship. The method of using the combination of partial function expansion and the plane wave expansion is explained in [31].

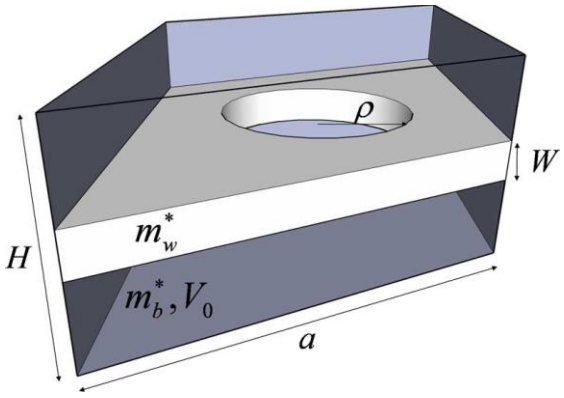

Figure 2.6 Unit cell of the IQD array [31].

Figure 2.6 shows the unit cell of the IQD array. In this figure, m_w^* and m_b^* are the carrier effective mass of the QW and barrier layers, V_0 is the potential across the barrier, H and W are the height of the unit cell and the width of the QW, a is the width of the unit cell, ρ is the pore position vector.

Let us define $\vec{u}$ and $\vec{v}$ as the unit vectors of the unit cell. Then, the reciprocal space vector G and the in-plane particle momentum vector k_t can be described using the reciprocal basis vectors u^* and v^* as shown in equations (2.14) and (2.15).

$$G = nu^* + mv^* \tag{2.14}$$

$$k_t = k_n u^* + k_m v^* \tag{2.15}$$

where n and m are the integers and k_n and k_m are the real numbers. The position vector is described in terms of the real space vectors as shown in equation (2.16).

$$\rho = u\vec{u} + v\vec{v} \tag{2.16}$$

The Schrödinger equation (2.17) can be simplified to equation (2.18) using the Bloch's theorem and equations (2.14) to (2.16).

$$-\frac{\hbar^2}{2m^*}\nabla^2\psi(u,v,z)+V(u,v,z)\psi(u,v,z)=E\psi(u,v,z) \tag{2.17}$$

$$\psi(u,v,z)=e^{ik_t\cdot\rho}u_{k_t}(u,v,z) \tag{2.18}$$

where m^* is the electron effective mass and V is the potential across the barrier. The envelop function $u_{k_t}(u,v,z)$ is the sum of the reciprocal lattice vector plane waves as shown below.

$$u_{k_t}(u,v,z)=\sum_{i,j}a_{i,j}(k_t)e^{iG_i\cdot\rho}f_j(z) \tag{2.19}$$

where $a_{i,j}$ is the Fourier coefficients and $f_j(z)$ is the normalized function along the z direction. In this case, $f_j(z)$ is approximated as the sinusoidal function shown in equation (2.20), because the structure of the IQD is similar to the QW along the transverse direction.

$$f_j(z)=\sqrt{\frac{2}{H}}\sin\left(j\pi\left(\frac{1}{2}-\frac{z}{H}\right)\right) \tag{2.20}$$

The Schrödinger equation (2.17) can be simplified using equations (2.18) to (2.20):

$$\sum_{i,j}a_{i,j}(k_t)M_{i,j,i',j^j}=Ea_{i',j'}(k_t) \tag{2.21}$$

The eigenvalues at each point of the Brillouin zone can be calculated by solving equation (2.21). The simulation using the combination of partial function expansion and the plane wave expansion in the IQD array has been reported by Verma in 2009 [31]. In this reference, the $In_{0.25}Ga_{0.75}As/GaAs$ active region with the hexagonally ordered pores is used. The diameter and the pitch between the pores are 40 nm and 80 nm respectively. The temperature is assumed to be 77K.

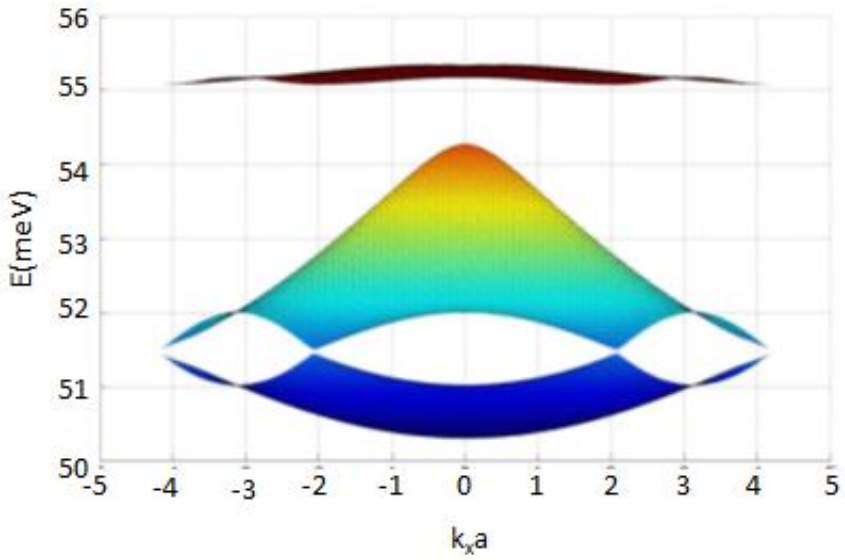

Figure 2.7 Simulated energy dispersion diagram of the first three conduction subbands in the transverse direction [31].

Figure 2.7 describes the energy dispersion diagram in the transverse direction including the first, second, and the third subbands. The forbidden energy gaps between the second and third subbands are greater than the energy gap between the first and second subbands.

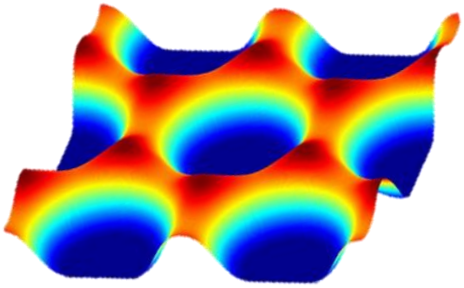

Figure 2.8 Simulated ground state diagram of hexagonally ordered IQDs.

Figure 2.8 shows the simulated tilted top view of the ground state in the hexagonally ordered IQDs. The probability of finding the electron increases going from the blue region to the red region.

From the energy dispersion calculation, the DOS can be derived as shown in equation (2.22).

$$\rho(E) = \frac{N}{V\Delta E} = 2 \times \frac{k_{Area} / (2\pi / L)^2}{L^2 W \Delta E} = \frac{k_{Area}}{2\pi^2 W \Delta E} \tag{2.22}$$

where k_{Area} is the reciprocal space area of the IQD, and $V = L^2 W$ is the unit volume in real space. As discussed in Chapter 1.1, the DOS is calculated by dividing the total number of energy states by the unit volume per energy level.

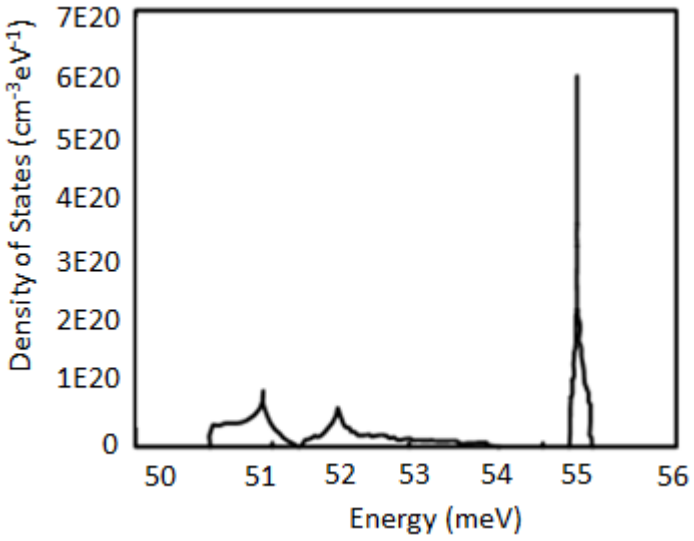

Figure 2.9 Simulated conduction band DOS of the IQD [31].

Figure 2.9 shows the simulated conduction band DOS of the IQD structure shown in Figure 2.8. The peaks of DOS at 51 meV, 52 meV and 55.4 meV correspond to the first, second and the third subbands of the conduction band. The first and second subbands are broadened due to the wavefunction overlapping. The forbidden energy gap between the second and third subbands is approximately 0.8 meV and there are no overlapping regions in energy dispersion

diagram. Therefore, the conduction band DOS in the third subband shows no broadening at 55.4 meV.

2.4 Photoluminescence (PL) Characterization

In this section, PL characterization of the IQD array is reported. The PL measurement directly shows the light emission spectrum of the structure. The comparison of the intersubband scattering between the QW and IQD has been reported by Dias in 2011 [36] and is described here.

The $In_{0.31}Ga_{0.69}As$ layer is used as an active region in both the QW and IQDs. The IQDs have hexagonal pore patterns with the diameter and pitch of 60 nm and 80 nm respectively. The PL measurement is performed using an Ar ion laser with 488 nm emission wavelength. The laser beam is focused on the sample, which is cooled down to 77 K using liquid N_2. The re-emitted photons from the sample are passed through a monochromator and detected using a liquid N_2 cooled Ge detector.

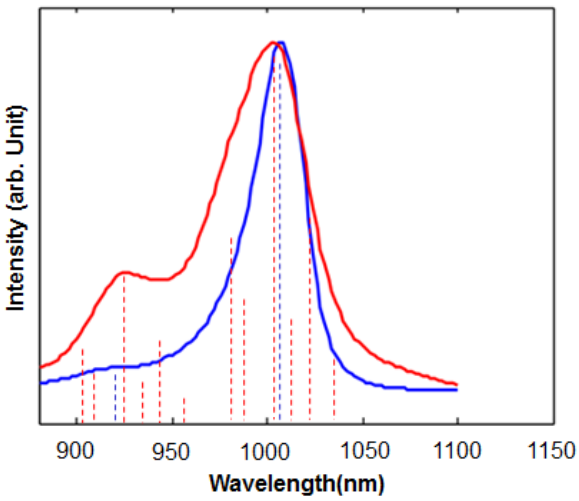

Figure 2.10 PL spectrum comparison between the $In_{0.31}Ga_{0.69}As$ QW and hexagonally ordered IQDs with pore diameter and pitch of 60 nm and 80 nm respectively.

Figure 2.10 shows the emission spectrum comparison between the QW and the IQDs. The first interband transitions in the QW and the IQDs occur at 1008 nm and 1004 nm respectively. This blue-shift of the IQDs emission spectrum proves stronger quantization of the electrons in the IQD structure. The second interband transition occurs at 928 nm for both the QW and IQDs, making it difficult to recognize the quantization. According to the report [36], the higher PL intensity of the second interband transition is caused by the reduced intersubband scattering. There are two possible reasons for the lower PL intensity of the second interband transition. The first reason is a carrier relaxation from the second to the first interband by the means of phonon scattering. The other reason is a direct electron-hole recombination. In the QW, a wavefunction overlapping between the first and second interband in z-direction causes the intersubband transition to dominate. In the IQDs, the wavefunctions overlapping in the transverse direction are minimized which reduces the carrier scattering.

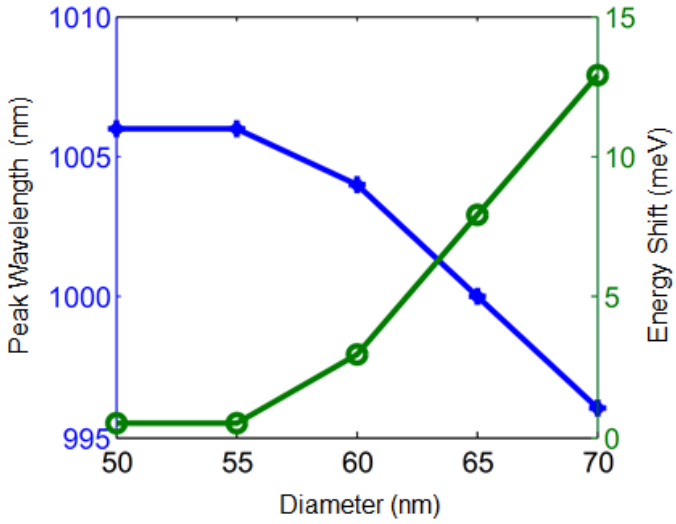

Figure 2.11 First Interband emission wavelength shift versus pore diameter [36].

The peak shifting of the first interband transition is reported to show the quantization dependence on the diameter of the pore as shown in Figure 2.11 [36]. In this experiment, the

$In_{0.31}Ga_{0.69}As$ active region with the pore pitch of 80 nm is used. The diameter of the pores is varied from 50 nm to 70 nm. The emission peak wavelength starts to blue-shift for the pores with the diameter of 55 nm. As the diameter increases from 55 nm to 70 nm, the peak emission wavelength decreases linearly. This result shows that the electron confinement can be controlled by varying the pore dimensions in transverse direction.

3. LARGE AREA FABRICATION

In contrast to the high precision and resolution given by the electron beam lithography, fabricating the nanostructure using the electron beam lithography is more expensive and time-consuming compared to the conventional photolithography. In this chapter, diblock copolymer (DBC) lithography and anodic aluminum oxide (AAO) pattern transfer are introduced as alternative techniques to the electron beam lithography to reduce the fabrication cost in mass production.

3.1 Diblock Copolymer Lithography

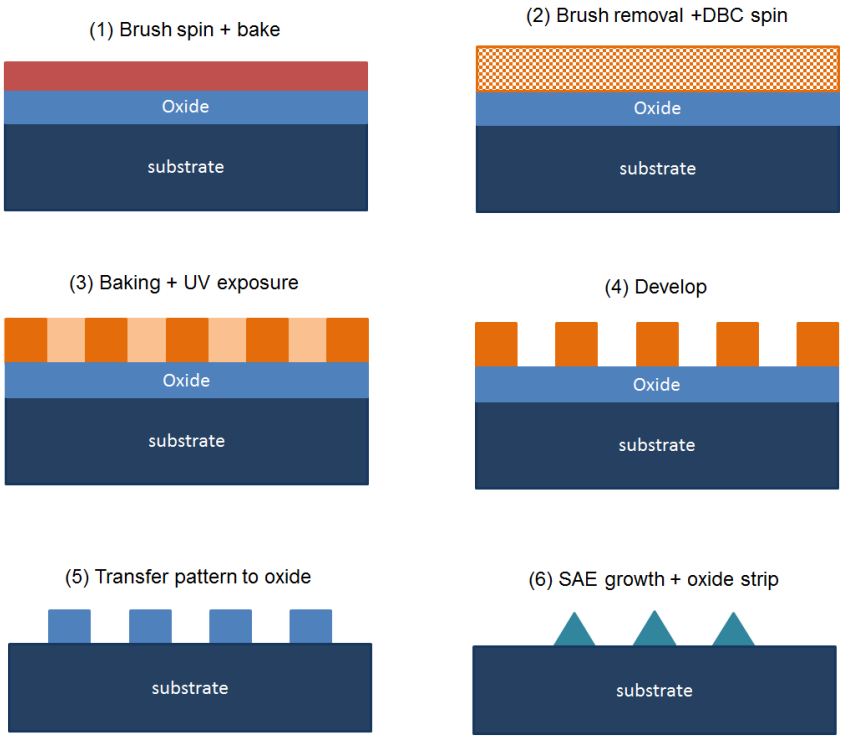

Figure 3.1 Fabrication processes of DBC patterned QDs.

DBC patterning process is schematically shown in the Figure 3.1. It consists of dot patterning on the DBC layer and pattern transfer to the dielectric film. A base structure is grown on a GaAs

substrate using the MOCVD. This base structure has a 100 nm GaAs buffer layer, a 300 nm $Al_{0.75}Ga_{0.25}As$ barrier layer, and a 10 nm GaAs confinement layer. An SiO_2 film is deposited using PECVD. Then, a brush layer is spin-coated to serve as the adhesive for the 20 nm to 40 nm thick DBC layer. In this experiment, we use PS-b-PMMA as the DBC material. Next, the DBC layer is exposed to ultraviolet (UV) radiation, baked, developed, and etched with the acetic acid to create the patterns. The pattern transfer to the dielectric film is performed using Freon-23 RIE etching. Before growing the QDs, the DBC layer is removed by immersing into acetone, methanol and isopropanol. The pores are etched in 1:1 HCL:DI to remove the native III-V oxide layer. After annealing the sample at 700 ℃ for 30 minutes to prevent dielectric mask damage, InAs QDs are grown at 450 ℃. The oxide mask is then etched using BHF.

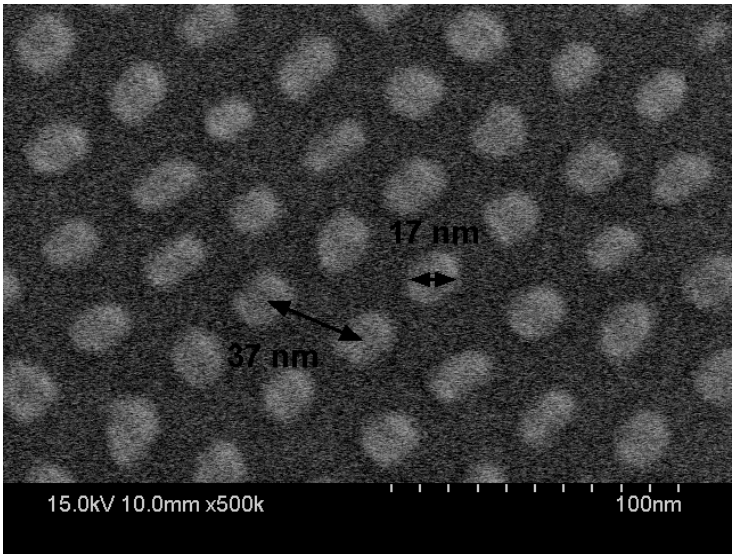

Figure 3.2 SEM image of Fabricated InAs QDs [37].

Figure 3.2 shows the top view SEM image of the InAs QDs. In order to find the distribution of the diameter, area, angle, and the aspect ratio of the QDs, an image processing algorithm is used.

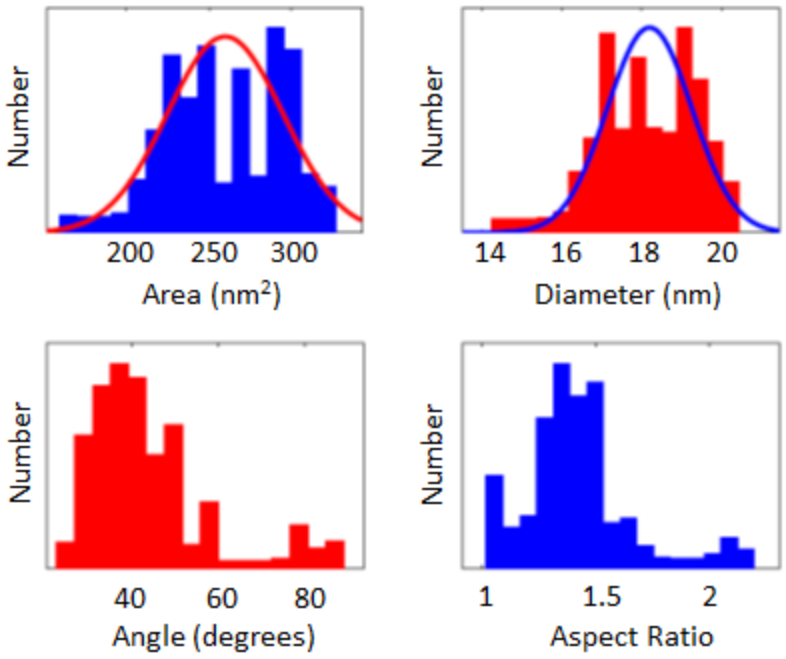

Figure 3.3 Image processing algorithm result for fabricated DBC patterned QDs [37].

According to the results shown in Figure 3.3, the average diameter of the InAs QDs is 18 nm with a standard deviation of 1 nm. The shape of the dots is elliptical with the average angle of 40 degrees, which is caused by the directional preference of the SAE process. This result shows improvement in uniformity over self-assembled InAs QDs which reportedly have a diameter variation of ± 10 nm. The density of the DBC patterned QDs is approximately 8.4×10^{10} cm^{-2} which is the highest density of patterned InAs QDs with MOCVD reported to date. The reported theoretical limit of the single layer QD density with the diameter of 20 nm in closed packed structure is 3×10^{11} cm^{-2} [38].

An atomic force microscope (AFM) is used to measure height of the InAs QDs. The average height of the QDs is 7 nm. Transmission electron microscopy (TEM) is required to accurately determine the final shape and the size of the QDs.

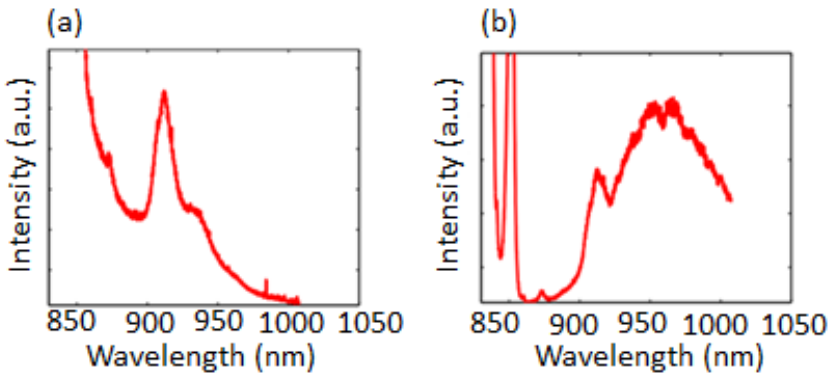

Figure 3.4 PL spectrum of self-assembled and DBC patterned $In_xGa_{1-x}As$ QDs. The PL spectrum of (a) annealed DBC QD, (b) annealed self-assembled QD.

Figure 3.4 shows the PL characteristic of self-assembled and DBC patterned $In_xGa_{1-x}As$ QD. Both self-assembled and SAE QDs are grown on the same GaAs substrate in different regions. A Ti:sapphire laser with 795 nm wavelength producing a spot size of 4 μm is used as the excitation source for the PL measurement at 4K [37].

Figure 3.4 (b) shows the PL spectrum with evidence of inhomogeneous broadening which was produced by the QD size fluctuation. The $In_xGa_{1-x}As$ peaks are shown at 935 nm, 952 nm, and 974 nm. Figure 3.4 (a) shows that the inhomogeneous broadening of the PL spectrum is reduced and showing a peak at 921 nm.

3.2 Anodic Aluminum Oxide Pattern Transfer

An anodic aluminum oxide (AAO) pattern transfer is a method to fabricate a dielectric film patterned with nanochannels [39]. The nanochannels can be turned into pores by etching the bottom of the channels. A nano-imprint template defines the size, the pitch and, thus, the density of the pores. Fabrication of highly ordered AAO pores with the density of 10^{10} cm^{-2} has been reported by Masuda in 1997 [40]. Pore fabrication using the AAO process is not as

complex and expensive as the process involving electron beam lithography. Using AAO to pattern the QDs or IQDs is a promising method for mass production of zero-dimensional structure devices.

AAO fabrication requires a nano-imprint template or a master mold and an aluminum film. A master mold is patterned on a SiC substrate using electron beam lithography. Figure 3.5 (a) shows a master mold placed above the aluminum film. The mold is pressed into the aluminum film by applying 5000 kg/cm^2 pressure, and consequently heated up to 400 ℃ as shown in Figure 3.5 (b). After removing the mold (Figure 3.5 (c)), the patterned aluminum film is anodized by applying a voltage while it is immersed into the oxalic acid solution (Figure 3.5 (d)). The AAO film is then transferred to the desired substrate.

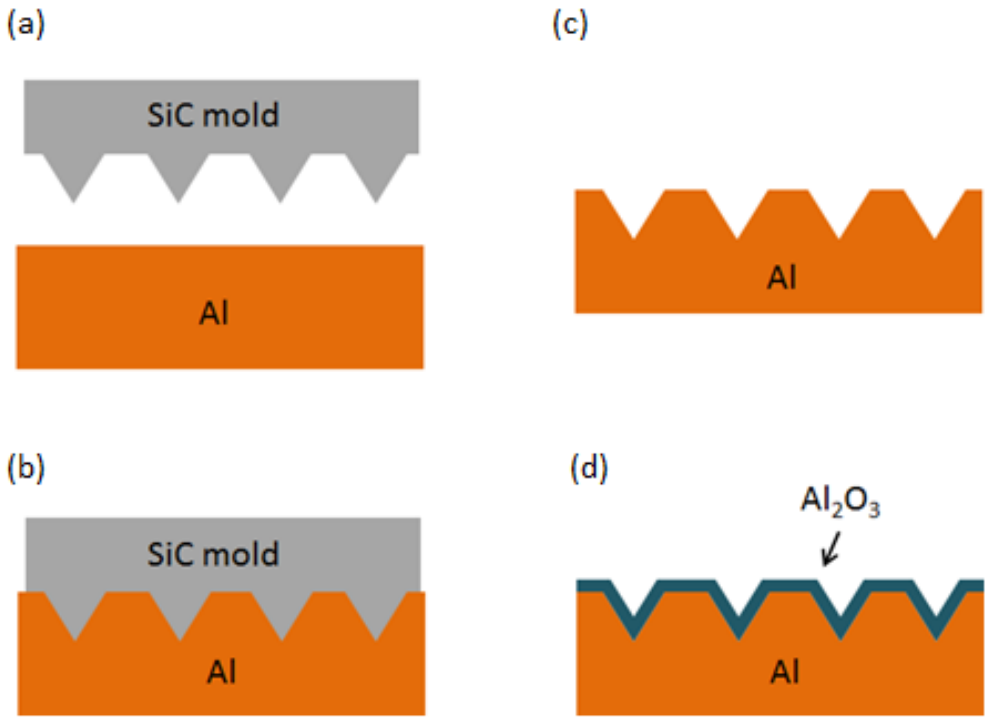

Figure 3.5 AAO fabrication process.

Figure 3.6 shows the fabrication steps for either QDs or IQDs using the AAO pattern transfer.

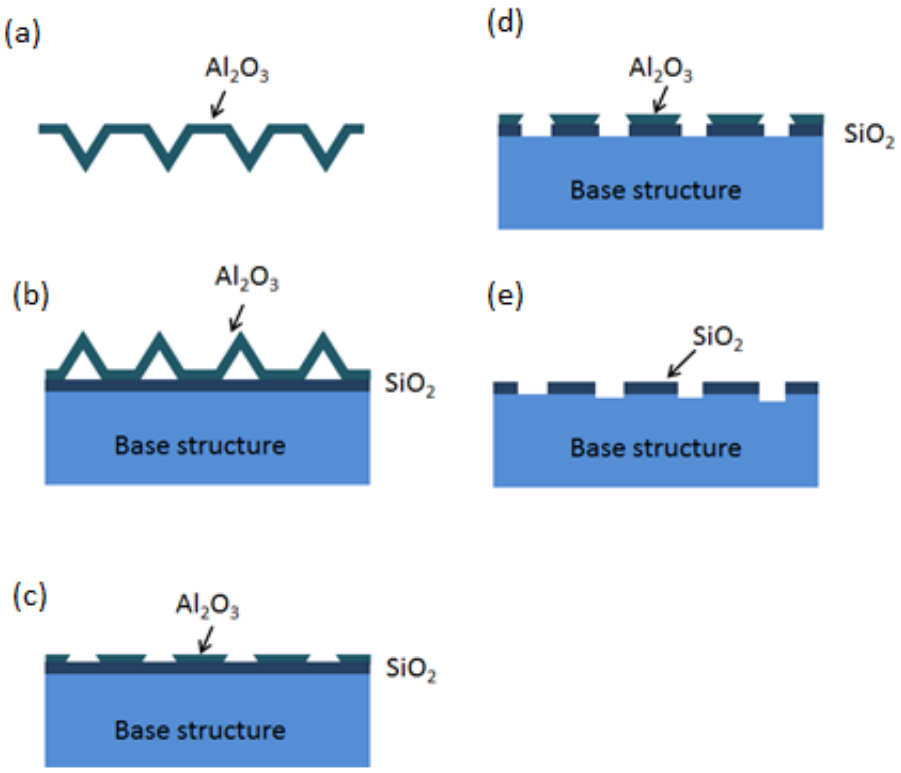

Figure 3.6 Steps for pattern transfer from AAO to SIO_2.

First, aluminum in the fabricated AAO is etched away with a saturated $HgCl_2$ solution leaving the Al_2O_3 film (Figure 3.6 (a)). Then, the Al_2O_3 film is placed on top of the QD or IQD base structure covered with a 30 nm SiO_2 film. The Al_2O_3 channels are opened using either a 3% wt H_3PO_4 solution or argon ion dry etching (Figure 3.6 (c)). The AAO pores are transferred to the SiO_2 film using Freon RIE (Figure 3.6 (d)). The remaining Al_2O_3 is removed using acetone, methanol and isopropyl alcohol under the sonication (Figure 3.6 (e)). At this point, the QDs or IQDs can be selectively regrown using MOCVD.

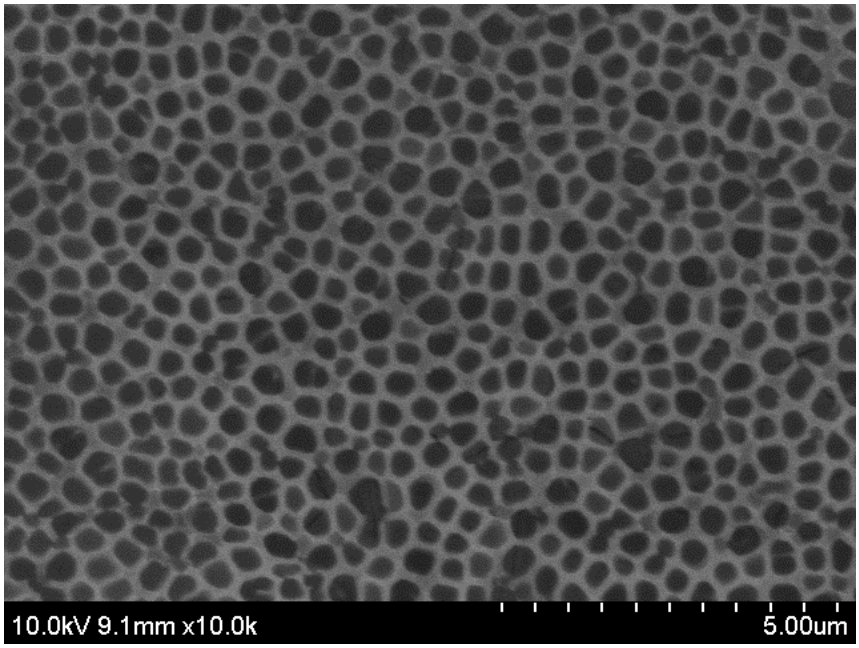

Figure 3.7 SEM image of wet etched AAO.

The wet etching shown schematically in Figure 3.6 (d) gives a non-uniform pore pattern (Figure 3.7). The average pore diameter and pitch of 100 nm and 500 nm respectively are obtained by etching the sample with H_3Po_4 solution for 3 minutes. QD or IQD cannot be grown in the under-etched or over-etched regions.

Figure 3.8 compares the morphology of the self-assembled InAs QDs and the selectively grown QDs fabricated under the same conditions. For both cases, the flow rates of 120 sccm TMIn and 90 sccm AsH_3 at 450 ℃ are used.

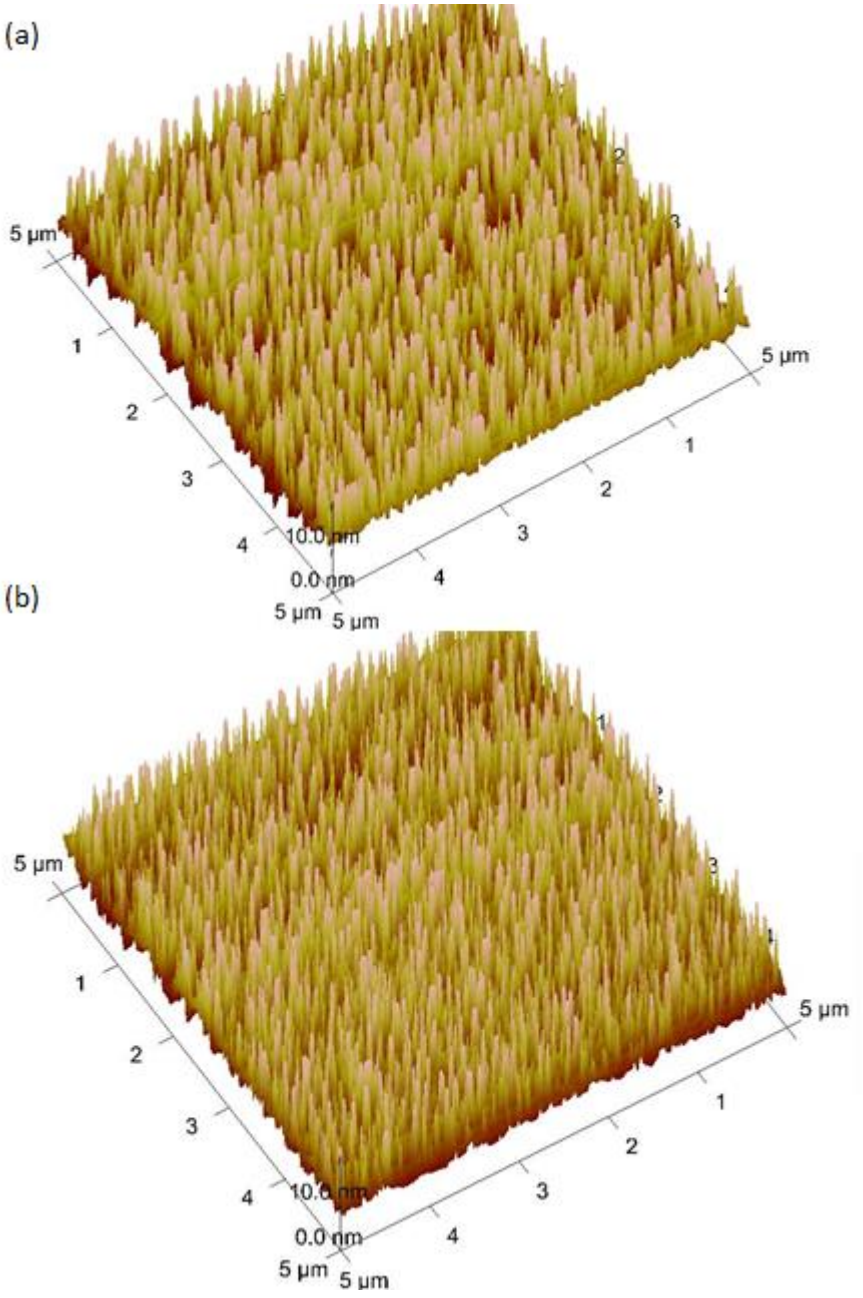

Figure 3.8 AFM image of (a) self-assembled and (b) AAO patterned InAs QDs.

The QD density in the AAO patterned sample is higher than that of the self-assembled QDs. While the AFM data gives the morphology of the surface, the structure of the QDs can be analyzed using the TEM.

As mentioned earlier, the wet etching may result in uneven surfaces and unopened pores, which can cause the non-uniform QD growth. Alternatively, argon ion milling can be used to solve the uniformity problem.

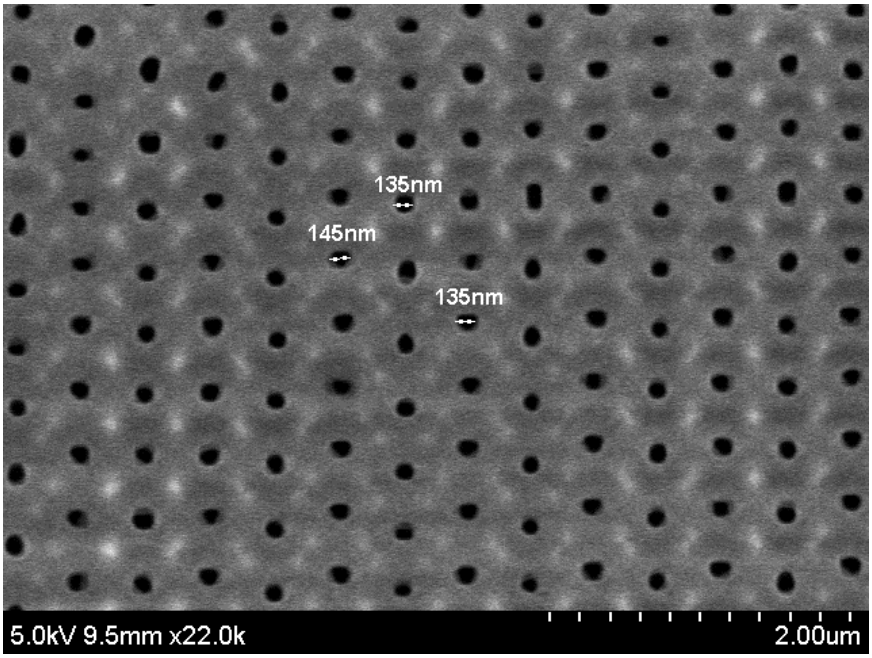

Figure 3.9 SEM image of SiO2 after pattern transfer from Ar ion milled Al_2O_3.

Figure 3.9 shows the SEM image of an SiO_2 film after the pattern transfer from Al_2O_3 using the argon ion milling for 5 minutes. The dry etch advantage over the wet etch can be seen by comparing Figures 3.7 and 3.9. An average pore diameter and pitch of 147 nm and 300 nm are observed respectively. To complete the wet and dry etch comparison, a regrowth step is done on the sample shown in Figure 3.9.

4. CONCLUSION

The ideal QD structure has enhanced optical characteristics. This 0D structure allows us to confine the carriers in all directions. In order for the QD industry to succeed, the uniformity of the size and density of the fabricated QD must be improved. Both the theoretical calculations and the experimental data of the QD show promising results for high efficiency optoelectronic devices. IQD is introduced as an alternative method to create the 0D structure. The uniformity of the size and the density of the QD can be enhanced by using the IQD structure. The methods of the large area QD and IQD array fabrication using the DBC and AAO techniques are described. These techniques are good alternatives to the electron beam lithography for cost effective fabrication of the 0D structures. Further research on the IQD and on fabrication of large area arrays of 0D structures is needed to make the IQD based devices suitable for commercialization.

REFERENCES

[1] L. V. Asryan and S. Luryi, “Tunneling-injection quantum-dot laser: ultrahigh temperature stability,” *IEEE Journal of Quantum Electronics*, vol. 37, no. 7, pp. 905–910, 2001.

[2] D. Bimberg, N. Kirstaedter, N. N. Ledentsov, Z. I. Alferov, P. S. Kop'ev, and V. M. Ustinov, “InGaAs-GaAs quantum-dot lasers,” *IEEE Journal of Selected Topics in Quantum Electronics*, vol. 3, no. 2, pp. 196–205, 1997.

[3] M. Asada, Y. Miyamoto, and Y. Suematsu, “Gain and the threshold of three-dimensional quantum-box lasers,” *NASA STI/Recon Technical Report A*, vol. 87, p. 16589, Sep. 1986.

[4] Z. Alferov, “Double heterostructure lasers: early days and future perspectives,” *IEEE Journal of Selected Topics in Quantum Electronics*, vol. 6, no. 6, pp. 832–840, 2000.

[5] Y. Arakawa and H. Sakaki, “Multidimensional quantum well laser and temperature dependence of its threshold current,” *Applied Physics Letters*, vol. 40, no. 11, pp. 939–941, Jun. 1982.

[6] R. J. Ellingson, M. C. Beard, J. C. Johnson, P. Yu, O. I. Micic, A. J. Nozik, A. Shabaev, and A. L. Efros, “Highly Efficient Multiple Exciton Generation in Colloidal PbSe and PbS Quantum Dots,” *Nano Lett.*, vol. 5, no. 5, pp. 865–871, May 2005.

[7] A. Marti, L. Cuadra, and A. Luque, “Partial filling of a quantum dot intermediate band for solar cells,” *IEEE Transactions on Electron Devices*, vol. 48, no. 10, pp. 2394–2399, 2001.

[8] A. Martí, E. Antolín, C. R. Stanley, C. D. Farmer, N. López, P. Díaz, E. Cánovas, P. G. Linares, and A. Luque, “Production of photocurrent due to intermediate-to-conduction-band transitions: A demonstration of a key operating principle of the intermediate-band solar cell,” *Phys. Rev. Lett.*, vol. 97, no. 24, p. 247701, Dec. 2006.

[9] “Quantum dots: global market growth and future commercial prospects,” BCC Research, NAN027C, Feb. 2011.

[10] L. V. Asryan and R. A. Suris, “Inhomogeneous line broadening and the threshold current density of a semiconductor quantum dot laser,” *Semicond. Sci. Technol.*, vol. 11, no. 4, p. 554, Apr. 1996.

[11] K. J. Vahala, “Quantum box fabrication tolerance and size limits in semiconductors and their effect on optical gain,” *IEEE Journal of Quantum Electronics*, vol. 24, no. 3, pp. 523–530, 1988.

[12] E. Bauer, “Phänomenologische theorie der kristallabscheidung an oberflächen. I,” *Zeitschrift für Kristallographie*, vol. 110, no. 1–6, pp. 372–394, Jan. 1958.

[13] F. C. Frank and J. H. van der Merwe, “One-dimensional dislocations. I. Static Theory,” *Proc. R. Soc. Lond. A*, vol. 198, no. 1053, pp. 205–216, Aug. 1949.

[14] J. H. V. D. Merwe, “Theoretical considerations in growing uniform epilayers,” *Interface Sci*, vol. 1, no. 1, pp. 77–86, Mar. 1993.

[15] B. Korgel and R. F. Hicks, “A diffusion model for selective-area epitaxy by metalorganic chemical vapor deposition,” *Journal of Crystal Growth*, vol. 151, no. 1–2, pp. 204–212, May 1995.

[16] V. J. Silvestri, R. Ghez, and T. O. Sedgwick, “Growth mechanism for germanium deposition near a SiO2 - Ge boundary,” *J. Electrochem. Soc.*, vol. 119, no. 2, pp. 245–250, Feb. 1972.

[17] D. G. Coronell and K. F. Jensen, “Analysis of MOCVD of GaAs on patterned substrates,” *Journal of Crystal Growth*, vol. 114, no. 4, pp. 581–592, Dec. 1991.

[18] M. Gibbon, J. P. Stagg, C. G. Cureton, E. J. Thrush, C. J. Jones, R. E. Mallard, R. E. Pritchard, N. Collis, and A. Chew, “Selective-area low-pressure MOCVD of GaInAsP and related materials on planar InP substrates,” *Semicond. Sci. Technol.*, vol. 8, no. 6, p. 998, Jun. 1993.

[19] M. Sugiyama, “Selective area growth of III-V semiconductors: From fundamental aspects to device structures,” *Indium Phosphide & Related Materials (IPRM), 2010 International Conference on*, pp. 1–6, May 2010.

[20] J. F. Kluender, A. M. Jones, R. M. Lammert, J. E. Baker, and J. J. Coleman, “Growth, characterization and modeling of InxGa1−xP stripes by selective-area MOCVD,” *JEM*, vol. 25, no. 9, pp. 1514–1520, Sep. 1996.
[21] A. M. Jones, M. L. Osowski, R. M. Lammert, J. A. Dantzig, and J. J. Coleman, “Growth, characterization, and modeling of ternary InGaAs-GaAs quantum wells by selective-area metalorganic chemical vapor deposition,” *JEM*, vol. 24, no. 11, pp. 1631–1636, Nov. 1995.
[22] J. S. C. Chang, K. W. Carey, J. E. Turner, and L. A. Hodge, “Compositional non-uniformities in selective area growth of GaInAs on InP grown by OMVPE,” *JEM*, vol. 19, no. 4, pp. 345–348, Apr. 1990.
[23] T. S. Yeoh, A. E. Huber, C. Y. Woo, R. B. Swint, C. Manzanedo, and J. J. Coleman, “InAs quantum dot selective area epitaxy using InGaAs thin films,” in *2000 IEEE International Symposium on Compound Semiconductors*, 2000, pp. 291–296.
[24] N. L. Dias, A. Garg, U. Reddy, J. D. Young, V. B. Verma, R. P. Mirin, and J. J. Coleman, “Directed self-assembly of InAs quantum dots on nano-oxide templates,” *Applied Physics Letters*, vol. 98, no. 14, pp. 141112–141112–3, Apr. 2011.
[25] H. H. Nilsson, J.-Z. Zhang, and I. Galbraith, “Homogeneous broadening in quantum dots due to Auger scattering with wetting layer carriers,” *Phys. Rev. B*, vol. 72, no. 20, p. 205331, Nov. 2005.
[26] U. Bockelmann, “Exciton relaxation and radiative recombination in semiconductor quantum dots,” *Phys. Rev. B*, vol. 48, no. 23, pp. 17637–17640, Dec. 1993.
[27] M. Sugawara, K. Mukai, and H. Shoji, “Effect of phonon bottleneck on quantum-dot laser performance,” *Applied Physics Letters*, vol. 71, no. 19, pp. 2791–2793, Nov. 1997.
[28] M. Sugawara, K. Mukai, Y. Nakata, H. Ishikawa, and A. Sakamoto, “Effect of homogeneous broadening of optical gain on lasing spectra in self-assembled $In_xGa_{1-x}As$/GaAs quantum dot lasers,” *Phys. Rev. B*, vol. 61, no. 11, pp. 7595–7603, Mar. 2000.
[29] M. Sugawara, K. Mukai, and Y. Nakata, “Light emission spectra of columnar-shaped self-assembled InGaAs/GaAs quantum-dot lasers: Effect of homogeneous broadening of the optical gain on lasing characteristics,” *Applied Physics Letters*, vol. 74, no. 11, pp. 1561–1563, Mar. 1999.
[30] V. C. Elarde and J. J. Coleman, “A novel ordered nanopore array diode laser,” *IEEE Photonics Technology Letters*, vol. 20, no. 4, pp. 240 –242, Feb. 2008.
[31] V. B. Verma, V. C. Elarde, and J. J. Coleman, “An analytical model for the ordered nanopore array diode laser,” *IEEE Journal of Quantum Electronics*, vol. 45, no. 1, pp. 10 –20, Jan. 2009.
[32] V. B. Verma and J. J. Coleman, “A parametric analysis of the density of states and intraband energy gaps in an ordered nanopore array diode laser,” *Journal of Applied Physics*, vol. 105, no. 4, pp. 043106–043106–8, Feb. 2009.
[33] J. M. Luttinger, “Quantum theory of cyclotron resonance in semiconductors: general theory,” *Phys. Rev.*, vol. 102, no. 4, pp. 1030–1041, May 1956.
[34] G. Bastard and J. A. Brum, “Electronic states in semiconductor heterostructures,” *IEEE Journal of Quantum Electronics*, vol. 22, no. 9, pp. 1625–1644, 1986.
[35] G. Bastard, “Superlattice band structure in the envelope-function approximation,” *Phys. Rev. B*, vol. 24, no. 10, pp. 5693–5697, Nov. 1981.
[36] N. L. Dias, A. Garg, U. Reddy, J. D. Young, K. P. Bassett, X. Li, and J. J. Coleman, “Experimental verification of reduced intersubband scattering in ordered nanopore lattices,” *Applied Physics Letters*, vol. 98, no. 7, pp. 071109–071109–3, Feb. 2011.
[37] N. L. Dias, “Patterned zero-dimensional nanostructures: fabrication and characterization,” Dec-2011. [Online]. Available: http://hdl.handle.net/2142/29771.
[38] K. Akahane, N. Yamamoto, and T. Kawanishi, “Fabrication of ultra-high-density InAs quantum dots using the strain-compensation technique,” *physica status solidi (a)*, vol. 208, no. 2, pp. 425–428, 2011.

[39] S.-F. Leung, M. Yu, Q. Lin, K. Kwon, K.-L. Ching, L. Gu, K. Yu, and Z. Fan, “Efficient photon capturing with ordered three-dimensional nanowell arrays,” *Nano Lett.*, vol. 12, no. 7, pp. 3682–3689, Jul. 2012.

[40] H. Masuda, H. Yamada, M. Satoh, H. Asoh, M. Nakao, and T. Tamamura, “Highly ordered nanochannel-array architecture in anodic alumina,” *Applied Physics Letters*, vol. 71, no. 19, pp. 2770–2772, Nov. 1997.